

Development of a hardware-in-the-loop wind tunnel setup to study the aerodynamic response of floating offshore wind turbines

Federico Taruffi¹ and Axelle Viré¹

¹Faculty of Aerospace Engineering, Delft University of Technology, Kluyverweg 1, 2629 HS Delft, the Netherlands

Correspondence: Federico Taruffi (F.Taruffi@tudelft.nl)

Abstract.

In floating wind turbines, the wind and wave excitation leads to motions of the floater affecting the rotor aerodynamic loads, which in turn influence the motion of the floater, in a highly coupled way. Numerical design tools can sometimes fail to predict certain aerodynamic phenomena, ~~such as the increase in thrust variation caused by unsteady effects. Thus and~~
5 ~~therefore~~, experimental testing is essential for tuning and validating these codes. Hybrid testing in wind tunnels, by measuring aerodynamic loads on a physical scale rotor under high-quality wind while numerically reproducing and actuating the floater motions, allows for higher fidelity in the reproduction of the aerodynamics compared to traditional wave basin tests. This work presents the development of a hybrid hardware-in-the-loop setup designed to study the aerodynamic response of floating wind turbines in wind tunnels. A scale model of a multi-megawatt floating wind turbine is mounted on top of a six degrees-
10 of-freedom hexapod robot. The full coupling of aerodynamic and floater dynamics is obtained with a hardware-in-the-loop approach with force-feedback-motion-actuation architecture. The rotor loads measured on the physical rotor are fed into a floater numerical simulator, which calculates the motion in real-time and actuates it through the hexapod. Key outcomes include the development of a hardware-in-the-loop numerical model with an aerodynamic loads estimation method to cope with scaling effects and the assessment of the floater simulator, the force estimation, and the measurement-actuation chain. The
15 aerodynamic effects on the motion response are preliminarily investigated on a 10MW floating concept, ~~with direct estimation of the rotor aerodynamic damping showing a 210% increase of damping in pitch with the turbine in operation~~ allowing to quantify the the increase in pitch, yaw, and surge damping through measured loads. The capability of testing combined wind and wave cases is also demonstrated, setting the framework for future studies.

1 Introduction

20 Offshore wind turbines are mostly installed as bottom-fixed structures rigidly mounted on the seabed or are moored to the seabed using floating support structures. In waters exceeding 60 meters in depth, floating turbines anchored on the seabed are more economical (van Kuik et al., 2016). As suitable shallow-water sites become increasingly scarce, floating offshore wind turbines (FOWTs) offer a promising alternative, unlocking the potential to harness vast wind resources in deeper seas and opening new opportunities in countries without shallow seas.

25 FOWTs experience (rigid-body) motions in six degrees-of-freedom (DOFs). The floating nature of the wind turbine makes it susceptible to various excitations, including changes in the met-ocean conditions, interactions between the wakes and the turbine, and the operation of the turbine itself. The aerodynamic performance of FOWTs is affected by these motions, with the aerodynamic loads acting on the rotor being highly coupled with the floater dynamics. In some cases, unsteady aerodynamic effects are observed due to the interaction of the wind turbine blades with their own wake. These complex interactions are often not yet fully understood. Current state-of-the-art is mostly limited to the analysis of a couple of degrees of freedom of the system under simplified met-ocean conditions.

It is currently challenging to numerically predict the flow physics around and behind floating rotors under certain conditions. The blade-element momentum theory is the reference engineering method to assess the performance of wind turbines. Despite the fact that corrections for rotor unsteadiness exist and have been successfully applied to the case of floating turbines (Papi et al., 2024), this low-fidelity approach cannot yet predict effects such as flow reversal and its impact on the rotor. Higher-fidelity methods, such as the free vortex wake model or computational fluid dynamics (CFD) method, have looked at both rotor unsteady loads and wakes, including returning wake effects (Schulz et al., 2024; Dong and Viré, 2022). However, some discrepancies between the results of high-fidelity numerical models and experimental data were recently found in predicting unsteady loads (Taruffi et al., 2024b). Additionally, the results from an experimental test were compared with the quasi-static theory which failed to predict the unsteady aerodynamic loading at high frequency (Taruffi et al., 2024a). This shows the need to better understand the unsteady phenomena associated with floating motions and derive more accurate tools for the design of FOWTs.

Experimental testing provides an effective way to investigate these complex phenomena and tune the numerical models. Full-scale testing or large-scale model testing can be done at sea. This was done by Viselli et al. (2015) with a 1:8 FOWT in the Gulf of Maine and by Ruzzo et al. (2021) with a 1:15 floating multi-purpose-platform including a wind turbine. However, this is expensive and the real offshore conditions are difficult to reproduce numerically. Hence laboratory tests with scaled models, which allow for a controlled testing environment, are often preferred. Testing FOWTs is traditionally done in a wave basin with Froude scaling. This allows for accurate hydrodynamic load reproduction, enabling the understanding of the floater hydrodynamics. For example, Cermelli and Aubault (2010) studied the hydrodynamics of a 1:67 scaled FOWT in a wave basin with Froude scaling to validate a numerical model. In order to include aerodynamic loading, wind generators with thrust disks or geometrically scaled blades were used to emulate the aerodynamic thrust force on the rotor. These methods successfully generated an aerodynamic thrust force but did not match the values of the full-scale model. The study by Goupee et al. (2014b) that involved testing a 5 MW wind turbine with different floaters in a wave basin with geometrically scaled blades revealed their drawbacks. This is due to the use of the Froude scaling law that does not allow for reproducing the aerodynamic forces correctly (Robertson et al., 2013). A Reynolds' similarity law would allow for accurate representation of the aerodynamics, but it compromises the gravity-related hydrodynamics loads, and anyway leads to impossibly high wind speeds. This scaling law conflict is unavoidable in fully-physical wave basin scale tests. To alleviate it, later studies followed a performance-based scaling methodology for the rotor for reproducing aerodynamic thrust more accurately while keeping the Froude scaling (Goupee et al., 2014a; Zhao et al., 2018; Doisenbant et al., 2018). Bredmose et al. (2017) also investigated different control

60 strategies in similar tests. However, this approach still has limitations, the main one being that the wind generators produce low-quality wind flows.

Hybrid testing can overcome these challenges (Shi et al., 2023). Instead of physically applying both the aerodynamic and hydrodynamic loading, one part is physically tested while the other is numerically simulated, effectively mitigating the scaling conflict, and allowing to test each part in the most appropriate laboratory. This can be done in wave basins where aerodynamic thrust is simulated with the help of winches or thrusters, or in a wind tunnel where an actuated platform is used to behave as the floater. The choice depends on the scope of the study, with the wave basin and wind tunnel setups meant to perform studies on hydrodynamics and aerodynamics respectively. Due to the high level of coupling between the aerodynamic loads acting on the rotor and the motion response of the floating system, hybrid tests where the numerical part contribution is pre-calculated may be suitable for specific studies, such as unsteady loads or wake measurements, but are not suitable to truly reproduce realistic conditions that are necessary to investigate the aerodynamic response and the stability of a design solution. To allow this, hardware-in-the-loop (HIL) technology is used, where the numerical part is simulated in real-time and accounts for the real-time measurements from the physical model to emulate the missing physics.

The first approach for real-time hybrid experimental testing in wave basins was developed with a ducted fan actuator by Azcona et al. (2014). The speed of the fan was adjusted to emulate different aerodynamic thrust forces. This methodology was later used to study the non-linear hydrodynamic effects of a FOWT as described in Azcona et al. (2019) and it overtook the traditional non-hybrid testing methods as it was confirmed to have better accuracy. Other researchers such as Oguz et al. (2018), Armesto et al. (2018) and Thys et al. (2018); Bachynski et al. (2016); Vittori et al. (2022) developed it further to include multiple fans or winch cables in order to better emulate aerodynamic forces and motions. These testing methods were used to verify and/or compare FOWT designs, tune numerical codes, or observe complex interactions, or tune numerical codes such as the one between the aerodynamic and hydrodynamic or mooring loads or the effect of the control system on the stability of the floater.

The HIL setup in wave basins allowed for validating floater designs and studying the complex dynamics. However, to analyse aerodynamic effects such as unsteady aerodynamics and wake interactions, experimental measurements on a physical rotor are required, and this is done with a complementary hybrid approach by testing in a wind tunnel. Hybrid testing in wind tunnel combines measurements on a physical scale rotor with higher-quality wind flow - high uniformity and stability and low turbulence intensity - when compared with the wind generators that equip wave basins, and reduces the Reynolds mismatch since Froude scaling is not mandatory, thus improving the fidelity in the reproduction of the aerodynamics. However, it is still necessary to use performance-scaled rotors because the Reynolds mismatch is still present. This approach presents some challenges, such as the difficulty in correctly scaling the rotor-nacelle assembly (RNA) mass, which demands a correction of the measured loads, and, as in the hybrid approach in the wave basin, ensuring real-time interaction between the physical and numerical parts. Wind tunnel hybrid/HIL testing was pioneered by Belloli et al. (2020), who developed a HIL setup with a 10 MW thrust-scaled wind turbine model mounted on a two DOFs slide first (Bayati et al., 2017) and a six DOFs hexapod later (Bayati et al., 2018b). A numerical model was developed to solve the floater dynamics, but still with limited force feedback (Bayati et al., 2018a). Recently, a 15 MW FOWT was tested with a 1:100 length scale with the same setup (Fontanella et al.,

95 2023b), and another setup has been developed by Jiang et al. (2025). There are many wind tunnel studies about aerodynamics and wakes using prescribed motions, without HIL coupling. Instead, research that used HIL testing in wind tunnels to study FOWT dynamics is scarce, given the few existing setups, and comparisons between different hybrid testing strategies and between tests in experimental facilities of different sizes are scarce.

100 This work adds to the current state-of-the-art by demonstrating a new hybrid testing setup capable of investigating a scaled rotor moving in all six DOF motions in a wind tunnel. The setup developed at Delft University of Technology uses a six DOF hexapod robot to emulate realistic floating motions. It was previously used to study prescribed motions imposed without coupling with the measured aerodynamics (Taruffi et al., 2024b). In this work, it is further developed to investigate the aerodynamic response of FOWTs using HIL technology. Key novelties include: the real-time motion coupling in six DOFs, including a new aerodynamic force estimation technique, a quantification of the aerodynamic damping effects on the turbine, and the
105 demonstration of the method application to realistic conditions.

The setup comprises physical aerodynamic loads that are fully coupled with numerically simulated floater dynamics. A numerical model is developed that solves the dynamics of the floater in six DOFs which includes estimating aerodynamic loads from the available measurements by applying a correction to the forces, and simulating the waves. Due to the scaling mismatch, the reliability of the force correction plays an important role in the accuracy of the setup for simulating real-world dynamics.
110 This work primarily focuses on the verification and validation of the setup, especially the force correction methodology, to ensure its accuracy to be utilised in future studies. An objective is to make the setup versatile enough to accommodate various FOWT designs, enabling the testing of larger turbines and different floater configurations with ease. Preliminary free decay and combined wind and wave tests are performed on a 10MW FOWT concept, investigating the aerodynamic damping effect on the motion response and assessing the capability of the setup to reproduce realistic wind and wave conditions.

115 **2 The hybrid setup**

The hybrid setup comprises a wind turbine scale model - the physical subsystem - and a six degrees-of-freedom hexapod robot - the numerical subsystem. The skeleton of the setup is the same as the previous work (Taruffi et al., 2024b) which focused on the study of rotor unsteady aerodynamics. In addition to the previous setup, a real-time controller bridges the two subsystems to implement the hardware-in-the-loop functionality.

120 This setup is for use in wind tunnels, and in this work, it is tested in the Open Jet Facility (OJF) at the Delft University of Technology, a closed-circuit open-jet facility with a $2.85\text{m} \times 2.85\text{m}$ octagonal nozzle opening into a 13.5m long, 6m wide and 6.5m high test section. The flow is uniform with a turbulence intensity of 0.5% at 1m from the jet exit, where the model is placed, and lower than 2% at 6m from it. The maximum wind speed is 35m/s and the temperature is kept constant by a heat exchanger. A complete characterization of the tunnel can be found in Lignarolo (2016). A view of the hybrid setup in OJF,
125 with its components highlighted, is shown in Fig. 1.

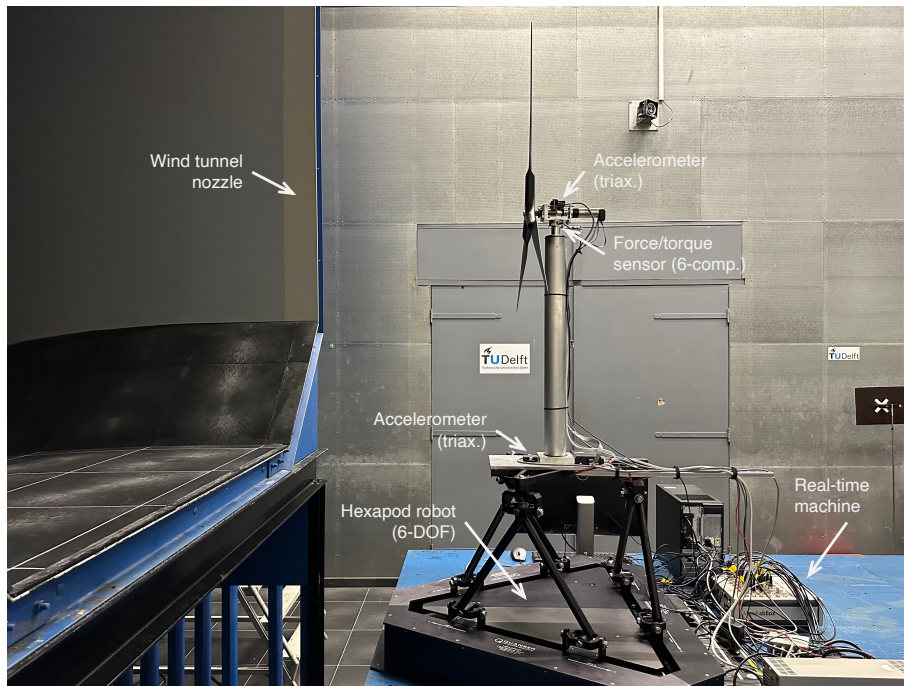


Figure 1. Picture of the setup and its components.

2.1 Wind turbine model

The scale wind turbine is a 3-bladed, fixed-pitch 1:148 model of the DTU 10 MW reference concept (Bak et al., 2013) operating with a velocity scale of 3. The rotor is designed by Fontanella et al. (2023a) with a performance-scaling approach aimed at correctly reproducing the thrust force, which is a common scaling objective for floating-related test models due to the predominant role of thrust in FOWTs motion. The relevant properties are reported in Table 1 and a complete experimental aerodynamic assessment, including both static and dynamic conditions, was performed in the previous study (Taruffi et al., 2024b). The experimental thrust curve is shown in Fig. 2 and ~~assesses the aerodynamic design of the rotor, proving its suitability to reproduce~~ proving the suitability for reproducing the full-scale rotor.

Table 1. Main wind turbine model specifications.

Parameter	Value	Unit
Rotor diameter	1.2	m
Hub height	0.8	m
Shaft tilt	0	deg
Nacelle mass	1.03	kg
Rotor mass	0.58	kg
Rated wind speed	4	m/s
Rated rotor speed	480	rpm

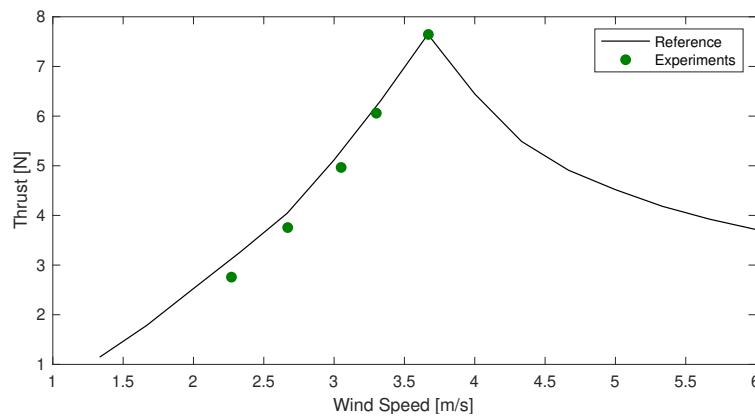


Figure 2. Rotor thrust from experiments (Taruffi et al., 2024b) compared with the nominal thrust curve of the full-scale turbine (reported at model-scale). The experimental points are averaged over two sets.

2.2 Hexapod

135 The motion system is the commercially available parallel kinematics robot Quanser Hexapod. The maximum velocity and acceleration are 0.67m/s and 9m/s^2 for translations and 80deg/s and 800deg/s^2 for rotations. The capabilities and limitations of the hexapod were evaluated with tests in the previous study (Taruffi et al., 2024b). A key outcome for this application is that the hexapod is capable of moving the wind turbine model at frequencies up to 5Hz (0.1Hz at full-scale or 1.5 in terms of reduced frequency) [with reasonable accuracy](#). The frequency range and acceleration limits are within the scaled motion

140 [range of 10MW FOWTs for most load conditions with an operational sea state. The window of interest is towards low-and wave-frequency ranges, while a response to tower and blades modes is out of the scope of this setup, considering that they are modelled as rigid.](#)

2.3 Instrumentation

The instrumentation system consists of several sensors and a real-time controller. A six-component load cell (model ATI
145 mini45 SI-290-10) installed between the tower top and the nacelle is used to measure the rotor integral loads and obtain the
aerodynamic forces. Two MEMS triaxial low-frequency accelerometers (model TE Connectivity 4030-002-120), one placed at
the hexapod-tower connection and the other one positioned on top of the nacelle, measure the translational accelerations. Both
are used to verify motion tracking, and the one on the nacelle is also used, together with the load cell, for the aerodynamic
force estimation process, as explained in Section 3.1.

150 The rotor is driven by a motor (model Maxon EC-4pole 30 200W) featuring a gearbox (model Maxon GP 32 C 5.8:1) and
connected to the rotor shaft with an Oldham coupler. The motor is controlled at constant speed by a servo drive (model Maxon
Escon 70/10) and equipped with a braking resistor (model Maxon DSR 70/30) to dissipate the power generated. The servo
drive provides the wind turbine operating data of rotational speed, measured by an encoder (model HEDL 5540) at the motor,
and torque, calculated from the motor current.

155 A real-time machine (model dSPACE 1302) is used to run the hardware-in-the-loop controller, chaining measurements and
actuation by simulating, in real-time, the floater dynamics (see Section 3). The unit is also used for data acquisition of all the
sensor signals and as human-machine interface to set test cases, command the operation of the turbine model and monitor the
signals. The real-time machine operates at 1kHz.

The wind speed is measured using a pitot tube installed in the tunnel nozzle. The speed at the testing location is also verified
160 with a portable fan-type anemometer.

2.4 Scaling of FOWT concept

This hybrid setup is designed to be scalable and represent different FOWT systems in the size range of 10MW with a scale
around 1:150. The rotor is a scale model designed for the DTU 10 MW reference wind turbine, but it can represent other rotor
ratings by adjusting the operating parameters according to the scale. Since the floater is represented by a numerical model, it is
165 virtually possible to use any platform and mooring design.

As introduced in Section 1, one of the key drivers of hybrid testing is to be able to reduce the Froude-Reynolds scale conflict.
For hybrid testing in wind tunnels, this translates into a custom scaling law (in Table 3) that comes as close as feasible to the
Reynolds scale bearing limitations given by the facility, the model manufacturing and the actuation system. The Reynolds
mismatch is reduced if compared to fully-physical testing in wave basin, however, a performance scale approach for the rotor
170 is still needed.

A non-Froude scaling introduces an acceleration mismatch which results in an incorrect reproduction of the balance between
inertial and gravitational phenomena acting on the wind turbine, while those acting on the floater are not affected as they are
numerically reproduced. Moreover, a mass mismatch is hardly avoidable at these scales due to production constraints resulting
in a manufacturable RNA mass around 10 times the scaled value. The combination of these scaling issues leads to large errors

175 and has to be numerically compensated by the hardware-in-the-loop setup for a correct reproduction of the full-scale dynamics,
as explained in Section 3.1.

A limitation on the size of the ~~FOWT-reproducible~~ reproducible FOWT is given by the scaling. Representing bigger concepts
with the same setup, as a 15 MW FOWT or more, increases the scaling effects. On the aerodynamic side, an increase in the
Reynolds number mismatch with the scale worsens the performance of the rotor. On the actuation side, the motion needs to be
180 quicker, approaching the limits of the hexapod in terms of motion frequency whose scaling is governed by $\lambda_f = \lambda_v \lambda_l^{-1}$ and
also challenging the hardware-in-the-loop chain latency.

Ultimately, an openly available 10 MW FOWT concept is chosen in this work with the scope of verification of the setup
itself. This is the DTU 10 MW with the SWE TripleSpar floater (Lemmer et al., 2016), whose design was validated in Bredmose
et al. (2017). The relevant properties of the concept are in Table 2. The load cases used as reference for the wave tests (in Table
185 5) are extracted from (Ramachandran et al., 2017) and refer to a site located in the Gulf of Maine.

Table 2. Properties of the FOWT concept from Bak et al. (2013); Lemmer et al. (2016)

Parameter	Value	Unit
Rotor diameter	178.3	m
Hub height	94	m
Rated wind speed	11.4	m/s
Rated rotor speed	9.6	rpm
RNA mass	612350	kg
Rated thrust	1619	kN
Rated power	10	MW
Floater mass	28828000	kg
Floater inertia, x	1.8674×10^{10}	kgm ²
Floater inertia, y	1.8674×10^{10}	kgm ²
Floater inertia, z	2.0235×10^{10}	kgm ²
Platform surge natural frequency	0.005	Hz
Platform heave natural frequency	0.06	Hz
Platform pitch natural frequency	0.04	Hz

Table 3. Non-Froude custom scale factors calculation and values.

Factor	Symbol	Formula	Value (fs/ms)
Length	λ_l		148
Velocity	λ_v		3
Frequency	λ_f	$\lambda_l^{-1} \lambda_v$	0.02
Acceleration	λ_a	$\lambda_l \lambda_v^2$	0.06
Mass	λ_m	λ_l^3	3241792
Reynolds mismatch	λ_{Re}	$\lambda_l \lambda_v$	444
Froude mismatch	λ_{Fr}	$\lambda_v \lambda_l^{-0.5}$	0.25

3 Hardware-in-the-loop

This setup's HIL architecture is of the type force-feedback-motion-actuation. The aerodynamic loads are measured on the physical model and are fed into the floater simulator, which calculates the next state of the system and actuates the hexapod, which moves accordingly. The floater simulator is a HIL numerical model developed in Matlab/Simulink environment to run in the real-time machine and it solves the dynamics of the floater in real-time by integrating the equation of motion at each time step, accounting for the measured aerodynamic loads, the numerically generated sea state and the hydrostatics, hydrodynamics and mooring system of the floater (see Section 3.2). The motions affect the measured aerodynamic loads, which in return affect the calculated motions at the next time step. This creates a loop and allows the two-way coupling of the rotor aerodynamics with the floater dynamic motions. A scheme of the HIL architecture is shown in Fig. 3.

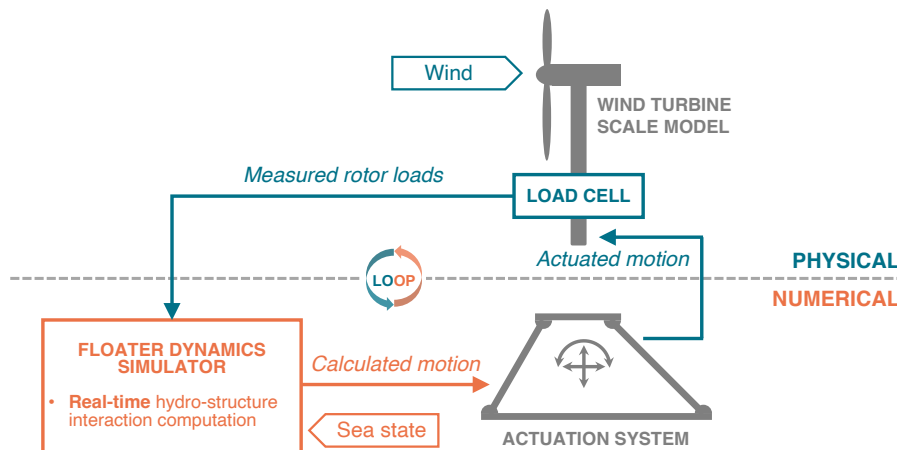


Figure 3. Scheme of the HIL architecture showing the force-feedback and motion-actuation chain.

Measuring pure aerodynamic loads with a load cell is not feasible for dynamic applications such as the one of interest here. The load cell measures at least the entire rotor load and, depending on where it is positioned, also the nacelle and tower loads. This includes aerodynamic, inertial and gravitational contributions. Similarly to Fontanella et al. (2023b), here the load cell used for the force-feedback is positioned between the tower top and the nacelle, instead of under the tower as in Belloli et al. (2020), and thus measures the loads acting on the RNA only. The advantage of measuring at the top of the tower is that the fraction of aerodynamic forces over measured forces is greater as the tower's inertial contributions, which are large given its non-scaled mass - the tower is designed as rigid - are not measured.

However, the measured rotor-nacelle forces cannot be directly used in the floater simulation and a correction procedure is necessary for two reasons. Firstly, the non-Froude scaling chosen for the setup (see Section 2.4) implies that the acceleration factor is not 1, thus the accelerations must be scaled; this applies also to the gravitational acceleration, which is not feasible to scale in experiments, leading to a gravitational acceleration mismatch between the physical and numerical parts of the experiment. Secondly, the mass of the rotor and nacelle cannot be scaled correctly due to manufacturing constraints that make it unfeasible for models in this scale range (1:100 - 1:200). This is due to the complexity of the RNA with the need for sensors, actuators and mechanical components, and the necessity of preserving the structural integrity of the scaled model, which poses critical requirements for the blade manufacturing. These acceleration and mass mismatches result in the misrepresentation of gravitational and inertial forces in the experiments. Since these forces are measured by the load cell together with the aerodynamic forces, which are not affected by misscaling, it is not possible to use the measurements as they are as feedback. To give an order of magnitude of the impairment, the acceleration mismatch of 15 and the mass mismatch of 10 lead to a mismatch in the ratio between the aerodynamic forces and the inertial and gravitational forces of 150. Aerodynamic forces and their effects being the focus of study in this setup, it is clear how this significant error would impair the experiments.

For this reason, a correction procedure is needed in real-time during the experiments. It is developed in this work, as described hereafter, and is performed by the HIL model. The measured loads are cleansed from the incorrect inertial and gravitational components and the estimated pure aerodynamic forces and torques are fed into the dynamic simulator, which numerically accounts for the true inertial and gravitational effects on the turbine together with the floater ones. In this work, it is not possible to apply a force correction a posteriori, as in Taruffi et al. (2024b), where the forces were corrected as a post-processing step because of the uncoupled nature of the prescribed motions. Here, the dynamics are fully-coupled and the measured loads are utilised in real-time to solve the floating motion, and therefore, the correction has to be done in real-time. The aerodynamic forces and torques are estimated as:

$$F_{aero} = F_{meas} - F_{corr}, \quad T_{aero} = T_{meas} - T_{corr}, \quad (1)$$

225

$$F_{corr} = F_{in} + F_{grav}, \quad T_{corr} = T_{in} + T_{grav}, \quad (2)$$

where F_{aero} and T_{aero} are the estimated aerodynamic forces and torques, F_{meas} and T_{meas} are the forces and torques measured by the load cell placed under the nacelle, F_{corr} and T_{corr} are the correction forces and torques, F_{in} and T_{in} are the inertia

forces and torques and F_{grav} and T_{grav} are the gravitational forces and torques. The forces and torques have three components
 230 each (x , y and z , where x is in the direction of surge, or along-wind, y is in the direction of sway, or lateral, and z is in the
 heave direction, or vertical). Thus, to obtain the aerodynamic forces, the inertial and gravitational forces that the load cell is
 measuring have to be estimated. This is done as follows:

$$F_{in} + F_{grav} = -M a_{meas}, \quad T_{in} + T_{grav} = -R^{-1} \begin{bmatrix} J_{rna,x} \ddot{\theta}_x \\ J_{rna,y} \ddot{\theta}_y \\ J_{rna,z} \ddot{\theta}_z \end{bmatrix} - \begin{bmatrix} M_{rna} a_{meas}(y) z_{lc} \\ M_{rna} a_{meas}(x) z_{lc} \\ 0 \end{bmatrix}, \quad (3)$$

where M_{rna} is the mass of the scale model RNA, J_{rna} is the moment of inertia, a_{meas} is the translational acceleration
 235 measured by the triaxial accelerometer placed at the nacelle, R is the rotation matrix (see Section A2) and z_{lc} is the vertical
 distance between the center of mass and the load cell sensor ($z_{lc} = 0.035\text{m}$), expressed in the rotating frame linked to the
 load cell. The value of M_{rna} is estimated at 1.6kg via system identification by actuating known motions and reading inertia
 forces with the same load cell as in the tests.

Using accelerations derived from the hexapod position feedback was found to be unsuitable, as it introduces errors due to
 240 the differentiation and operation and the time delays between the load cell sensor signals and the hexapod feedback. Instead,
 the signals measured by the accelerometer placed at the nacelle are utilised. The advantage is-lays-lies in the usage of a
 direct measurements taken at the location where the forces are also measured, therefore reducing latencies between the two
 and transformation errors. A limitation of this implementation is the neglect of the inertia torque terms $J_x \ddot{\theta}_x$, $J_x \ddot{\theta}_y$ and $J_x \ddot{\theta}_z$
 $J_{rna,x} \ddot{\theta}_x$, $J_{rna,y} \ddot{\theta}_y$ and $J_{rna,z} \ddot{\theta}_z$ because of the lack of a reliable source for $\ddot{\theta}_x$, $\ddot{\theta}_y$ and $\ddot{\theta}_z$ given that no rotational acceleration
 245 are measured. The force correction analysis (see Section 3.3.2) proves that this does not affect the roll and pitch directions,
 where the translational acceleration term $M a_{meas}$ is dominant. There is essentially no correction in the yaw direction, but
 this does not seem to affect the response. After the correction, the estimated aerodynamic forces are transformed from the
 rotating reference frame centered at the nacelle to the non-rotating reference frame centered at the FOWT still water level,
 corresponding to the tower base of the model, used as origin in the floater dynamic model.

250 3.2 Floater dynamics

A numerical model is developed to simulate the floater dynamics. This model takes as input the estimated aerodynamic forces
 and computes the motion response of the FOWT in six degrees-of-freedom returning as output the position to be imposed
 on the hexapod. A compromise between fidelity and computational cost has to be made to ensure the capability of running
 the model in real-time. Thus the modelling follows a mid-fidelity approach, similar to the widely-used simulation tool FAST
 255 (Jonkman and Buhl, 2005) and previous HIL setups (Belloli et al., 2020). The focus of this setup is on the motion-induced
 aerodynamic loads and the floater dynamics have to be reproduced sufficiently accurately to produce realistic motions, by
 which the aerodynamics are affected. The focus of this study is not on analysing the details of hydrodynamics or mooring
 effects. For this reason, a higher-fidelity hydrodynamic model (e.g. computational fluid dynamics) is out of scope and not
 feasible given the real-time constraints.

260 The motion response - in physics-based models - is determined by solving the equations of motion. For FOWTs, this is commonly done with a derived version of the Cummins equation (Cummins et al., 1962), which models the complete dynamics of the floater as a damped spring-mass system subjected to external forces, such as aerodynamics, hydrodynamics, and mooring forces. The model used here is targeted at semi-submersible floaters, and the equations of motion are given by:

$$M\ddot{x} + R\dot{x} + Kx = F_{\text{hydro}} + F_{\text{moor}} + F_{\text{aero}}, \quad (4)$$

265 where M is the structural mass, R is the linearised viscous damping, and K is the total stiffness. All are 6×6 matrices. The external 6×1 force vectors are: F_{hydro} for the hydrodynamic force, and F_{aero} for the aerodynamic force. Additionally, x is the position coordinates vector, \dot{x} is the velocity vector, and \ddot{x} is the acceleration vector. The stiffness terms include the gravitational (K_{grav}), the mooring (K_{moor}) and the hydrostatic contributions (K_{hst}). A comprehensive equation of motion is detailed in Appendix A4.

270 The hydrostatic and hydrodynamics are modelled using the potential flow theory. The effects considered are hydrostatic restoring, radiation loads and first-order incident wave diffraction. Their calculation relies on panel code (e.g. WAMIT) simulation outputs representing the floater's hydro-properties. The hydrostatic restoring contribution is accounted for in the stiffness matrix of the system, while the infinite-frequency added mass is in the mass term. The first-order diffraction forces, the total first-order wave excitation including the Froude-Krylov and scattering components as for Newman interpretation, are pre-
275 calculated based on the sea state corresponding to the test case and use the JONSWAP spectrum for irregular waves with WAFO tool (Brodtkorb et al., 2000). The radiation forces instead need to be calculated in real-time. Normally, a convolution integral needs to be computed to keep the memory effect, however, given the real-time application, a state-space approximation is preferred. The state-space model parameters are identified using a state-space identification tool developed by Duarte et al. (2013). A linear approach is used for the mooring lines in the form of a stiffness matrix.

280 The properties of the selected concept relevant to building the dynamic model are in Table 2 and are obtained from Lemmer et al. (2016) and Lemmer et al. (2020), where the hydro-properties are available. As detailed in 3.3.1, the model is then tuned with FAST (v8.16) as benchmark.

3.3 HIL assessment

Prior to wind tunnel testing, the HIL setup is assessed in cases without wind to ensure the trustworthiness of the results in
285 wind cases. Both the dynamic model and the HIL architecture itself, namely the measurement and actuation loop and the force correction method, are verified. This is done following a methodology that can be considered a best practice for hardware-in-the-loop wind tunnel testing and covers three steps of assessment and measurements:

1. Tuning and verification of the dynamic model
2. Verification of the measurements, correction and actuation loop
- 290 3. Aerodynamic measurements

3.3.1 Floater simulator

Step 1 is to verify the dynamic model simulating the floater. This is done by performing standalone simulations in Simulink and it corresponds to testing in *Open-Loop*, i.e. without force feedback. It is to assess the modelling of the FOWT rigid body dynamics, hydrodynamic and mooring. FAST is used as benchmark for comparison. In this step only, the simulations are performed at full-scale on a non-real-time machine, and the robot is not connected. Therefore, only the result of the simulation is considered, not the motion of the hexapod.

The rigid-body dynamics are determined with free decay simulations individually for each degree-of-freedom. Free decays are commonly used to characterize the rigid-body dynamics of floating systems, from which the natural frequency and linear damping ratio are evaluated. The simulations, both in Simulink and FAST, are run with no wind and no rotation of the rotor. The mooring is simulated dynamically in FAST using MoorDyn module, while linearly in Simulink.

The dynamic model is fine-tuned adjusting the damping and stiffness term to match the FAST simulations. This tuning process is done iteratively and for each degree-of-freedom. Damping requires adjustments because the HydroDyn modelling of the FAST module is more complex, while stiffness requires it as a linear mooring model is tuned with a nonlinear model. Small initial conditions (2m for translational DOFs and 2deg for rotational DOFs) are used to stay within a fairly linear range in the mooring reproduction in the benchmark.

The comparison between the decays for each DOF can be seen in the time domain in Fig. 4, where the tuned dynamic model closely resembles the response of FAST, and the obtained values of natural frequency and damping ratio, the latter using the logarithmic decrement, are reported in Table 4. Overall, the decay responses match satisfactorily.

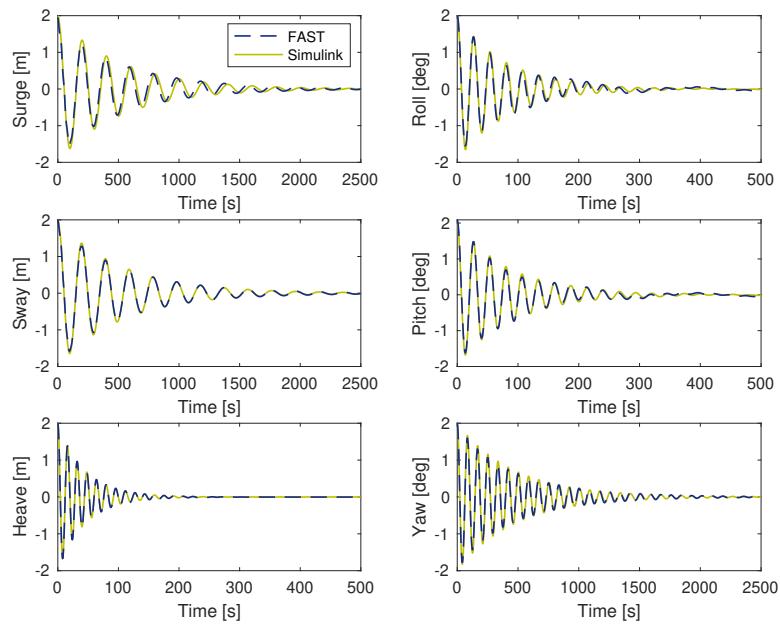


Figure 4. Time histories of floater DOFs for decay simulations with FAST (benchmark) and with the standalone HIL numerical model.

The wave response is evaluated with simulations in wave conditions, using case 4 from Table 5. The comparison is performed
 310 in the frequency domain given the different random seeds used for wave generation. The motion PSD for the DOFs affected by wave forces, namely surge, heave, and pitch, in Fig. 5 shows a satisfactory match.

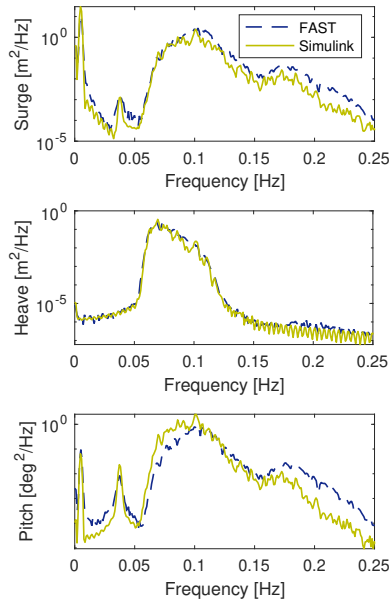


Figure 5. PSD of floater motion response to wave loading ~~for decay of~~ simulations with FAST (benchmark) and with the standalone HIL numerical model.

3.3.2 HIL setup

With the verified dynamic model, step 2 is to assess the HIL architecture itself and specifically the force-feedback and motion-actuation chain with the force correction procedure. To assess it, it is necessary to isolate its effect. This is done by testing in
 315 *Closed-Loop* - with the force feedback activated - and comparing the same case tested in *Open-Loop* - simulation without force input. Free decay cases in each DOF are performed in no-wind and no-rotation conditions so that the only difference with the open-loop tests is the activation of the force feedback. Since there is virtually no aerodynamic force involved, considering that the aerodynamic force developed by the non-rotating rotor is small, ideally the motion response in *Closed-Loop* should exactly match the *Open-Loop*. This implies that the loop and the force correction work correctly and all the rotor non-aerodynamic
 320 loads, which are undesired inertia and gravitational forces measured by the load cell in the closed-loop configuration only, are cancelled out correctly. An incomplete or wrong correction would result in a different motion response, for example, an amplification or a change in natural frequency and damping.

The comparison is shown in time domain in Fig. 6, and Table 4 reports natural frequency and damping values. The open-loop and closed-loop tests match closely. Even the response in yaw, although the total lack of force correction in this DOF as
 325 explained in 3.1, shows discrepancies only after a few cycles. The error of neglecting the correction is still present and could become significant for other load cases; however, this study tests cases with aligned wind and waves, where the yaw response is expected to be small and, for this reason, the error has a limited impact. The response of the other rotational DOFs, roll

and pitch, ~~is not visibly~~ does not seem to be affected by the incomplete correction they are subject to. The pitch decay with closed-loop appears more damped in the first cycles, but this effect can be attributed to the drag of the non-spinning rotor being non-null and dampening the pitch motion in the first cycles where the hub velocity is high, given the big initial condition tested. This is the only difference between pitch and roll, which match well, that could explain the discrepancy.

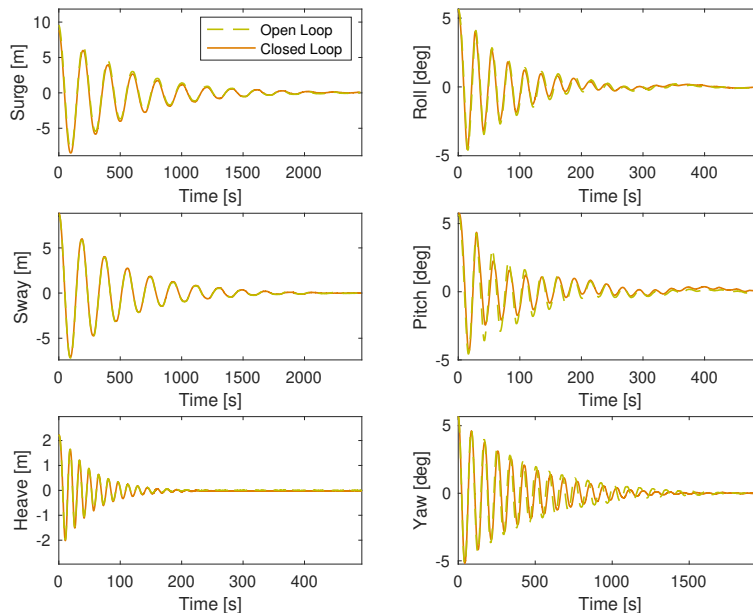


Figure 6. Time histories of floater DOFs for decay tests with the HIL setup in *Open-Loop* and *Closed-Loop* configuration. The results are upscaled.

An analysis of the force correction breaks down how the methodology is applied by the HIL with actual signals. It shows the correction of along-wind force F_x and torque T_y for a pitch decay without wind. This is the most relevant case because F_x and T_y are in the direction of wind, and thus of thrust, pitch shows faster oscillations than surge and is therefore more critical, and the no-wind case allows for an easier understanding of the performance of the correction, given that a good correction is achieved when the estimated aerodynamic force is zero. In Fig. 7, the bottom plot shows the pitch decay time history. The top plot shows the estimation of the aerodynamic force in the along-wind direction: the blue solid line is the measured rotor force $F_{meas,x}$, the red solid line is the correction, and the green line is the aerodynamic force $F_{aero,x}$ estimated by the model. As desired, the estimated aerodynamic force is approximately null. The mid plot shows the estimation of aerodynamic torque in the along-wind direction, about the tower base: the blue dashed line is the measured rotor torque $T_{meas,y}$, the red dashed line is the signal used to correct it, the blue solid line is the measured rotor force $F_{meas,x}$ multiplied by the hub height (to calculate the torque at tower base), the red solid line is the signal used to correct it, and the green line is the aerodynamic torque $T_{aero,y}$ estimated by the model. Despite, in theory, the blue dashed contribution is not entirely corrected by the red dashed contribution

due to the neglect of the rotational acceleration term, the two are almost indistinguishable because. Moreover, it is visible that the impact of the force arm is predominant when the moments are transported about the tower base, making the correction of $F_{meas,x}$ more important than the correction of $T_{meas,y}$. Overall, the estimated torque is also approximately null, and this proves the negligible effect the incomplete correction has. The visualisation of the correction of other force components and of cases with wind is reported in A6.

Altogether, this assesses the HIL system, mainly the force correction procedure, and can give an indication of the expected accuracy of the results obtained in the wind tests.

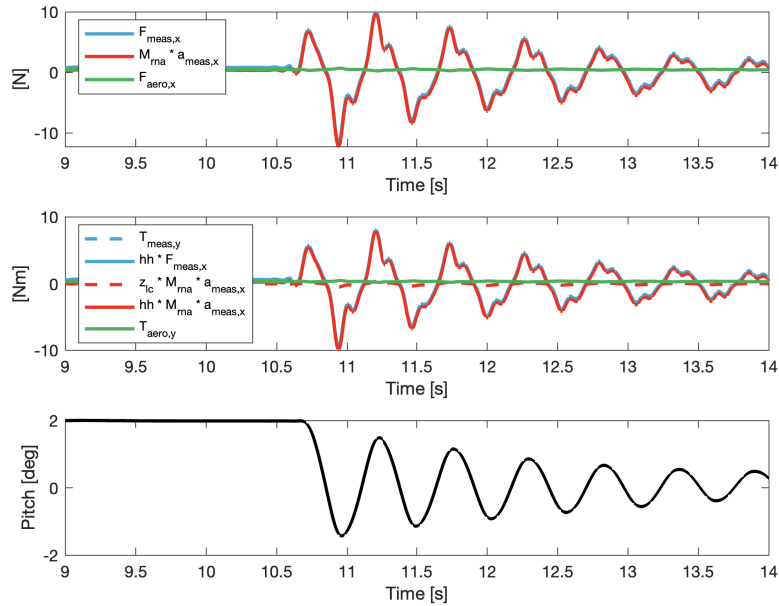


Figure 7. Force correction in the along-wind direction for a pitch decay without wind.

3.3.3 Real-time limitations

Keeping the real-time in the floater simulation and ensuring that delays don't compromise the stability of the system are of fundamental importance. The real-time machine integrates the HIL model with a time step of 1ms and no delay compensation is implemented. No filter is applied to the force and acceleration inputs because all the filter and cut-off frequencies tested resulted in an unstable HIL system. The force and acceleration sensors show no visible lag between their signals, as shown in Fig. 7. This improves the force correction process, because of the approach of using measured rather than derived signals for it. The sensors are used within their response range, i.e. 0 – 200Hz for the accelerometer and higher for the force sensor, whose bandwidth is given by the resonant frequency, which is around 5000Hz, from which a usable range of approximately 0 – 1000Hz is assumed. The actuation latency of the hexapod is estimated considering the delay between the position command

360 from the real-time machine to the hexapod and the position feedback from the hexapod to the real-time machine, and the latency
between the command and actual motion is assumed to be half of it. The total latency between the physical phenomena, i.e.
the aerodynamic loads acting on the rotor, and the motion that it induces is estimated ~~as about 50ms~~ to be less than 100ms. To
evaluate the motion tracking of the hexapod, the transfer function between position setpoint and actual position is also estimated
and it is reported in A5. For the sake of being conservative, the estimated delay includes the phase shift of the actuation at the
365 upper frequency limit of 5Hz.

4 Aerodynamic response

After assessment of the HIL setup, aerodynamic measurements can be performed with wind tunnel tests as step 3. This work
has its focus on the HIL setup development and assessment, thus a limited amount of tests and analyses are carried out. The
aim is to explore the potential of the HIL setup ~~of for~~ for investigating the aerodynamic response of FOWTs. Decay tests are run to
370 experimentally estimate the aerodynamic damping of the rotor and a set of realistic combined wind and wave cases are tested
to study the wind and turbine effects on the floater motion response. The aerodynamic tests are performed in wind conditions
and with the turbine rotor spinning at a fixed speed. The HIL feedback system is always active (*Closed-Loop*).

4.1 Aerodynamic damping

With HIL, the floater motion is not pre-calculated but computed in real-time based on the measured aerodynamic loads. Thus,
375 it is straightforward to quantify the effect of the rotor aerodynamic damping on the floater motion response and estimate the
aerodynamic damping itself. This is achieved by performing *Closed-Loop* decay tests in wind conditions for each DOF and
comparing the results with no-wind decays. From the comparison, the effect of the rotor aerodynamics can be investigated
and the aerodynamic damping can be quantitatively estimated. These cases are performed with the turbine operating at rated
conditions (wind speed of 4m/s and rotor speed of 480rpm).

380 The time domain comparison is shown in Fig. 8 and a frequency domain analysis is in Fig. 9. From the later, the natural
frequency of each DOF is visible as the highest peak. Before the peak of the natural frequency, there is another peak visible
in roll and pitch. This smaller peak is the natural frequency of sway and surge, respectively. This peak is visible due to the
coupling between roll and sway, and pitch and surge. The smaller peak around 8Hz in heave and roll is the 1P frequency of the
rotor, visible only in these DOFs.

385 The spectra with wind show peaks that are lower and broader for surge, pitch and yaw degrees of freedom. This implies that
the rotor provides damping, as qualitatively explained hereafter. Assuming rotor speed and blade pitch are fixed as in the tests,
the rotor moving against the wind direction in surge or pitch motions results in an increase in thrust force due to the increase in
relative wind speed seen by the rotor. When the rotor is moving in the direction of the wind, the thrust force decreases for the
same reason. The increase and decrease in thrust force oppose the motion, slowing down the oscillation with a damping effect.
390 A similar phenomenon explains the damping in yaw oscillation, where the part of the rotor that moves against the wind during
the yaw rotation sees an increase in relative speed, and consequently an increase in force in the wind direction which opposes

the rotation. On the other side of the rotor, the opposite happens (a decrease in relative wind speed and a consequent decrease in force, which again opposes the rotation), ultimately causing the damping effect. A quantitative analysis is done to estimate the aerodynamic damping effect on DOFs natural frequencies and damping, repeating the decay tests for three initial conditions, calculating the damping ratio with the logarithmic decrement and averaging the results, which are reported in Table 4. The pitch DOF is the most largely affected, showing an average increase in the damping of ~~220%~~ 210% in rated wind compared to no-wind. This is followed by yaw with 52% increase and surge with 19%.

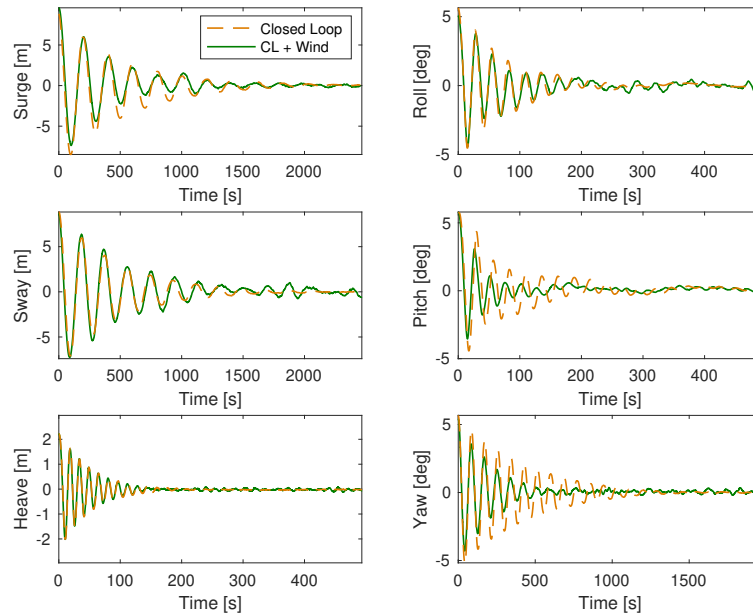


Figure 8. Time histories of floater DOFs for HIL (*Closed-Loop*) decay tests in *no-Wind* and *Wind* conditions. The results are upscaled.

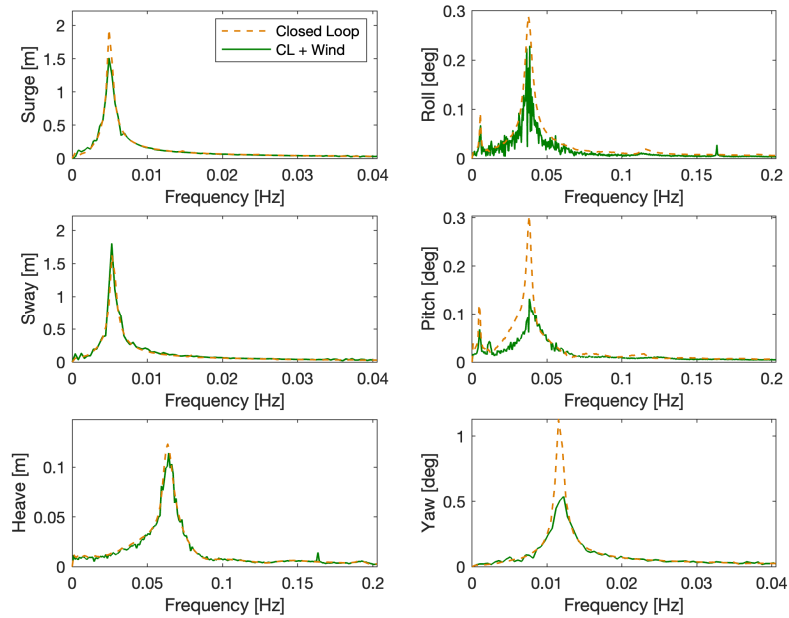


Figure 9. Frequency spectra of floater DOFs for HIL (*Closed-Loop*) decay tests in *no-Wind* and *Wind* conditions. The results are upscaled.

Table 4. Natural frequencies and damping ratios of the floater DOFs obtained from decay cases with FAST, with the HIL model and in the HIL tests in *Closed-Loop* and *Closed-Loop & Wind* configurations. The values of *Closed-Loop* and *Closed-Loop & Wind* are averaged over three different initial conditions and are upscaled to full-scale for the comparison. The last column shows the effect of aerodynamic damping in wind-aligned DOFs.

DOF	FAST		HIL Model		Closed-Loop		Closed-Loop & Wind		
	Nat. Freq. [Hz]	Damp. [-]	Nat. Freq. [Hz]	Damp. [-]	Nat. Freq. [Hz]	Damp. [-]	Nat. Freq.[Hz]	Damp. [-]	Aero. Damp. [%]
Surge	0.0050	0.056	0.0050	0.062	0.0050	0.069	0.0051	0.082	+ 19
Sway	0.0051	0.057	0.0051	0.059	0.0054	0.066	0.0054	0.043	
Heave	0.063	0.058	0.063	0.058	0.065	0.051	0.065	0.043	
Roll	0.038	0.059	0.037	0.054	0.037	0.059	0.037	0.074	
Pitch	0.038	0.059	0.037	0.050	0.038	0.047	0.040	0.15	+ 210
Yaw	0.012	0.032	0.012	0.029	0.012	0.035	0.012	0.054	+ 52

4.2 Wind and wave tests

Combined wind and wave cases are tested to demonstrate that the setup is suitable for reproducing realistic loading conditions. 400 Five irregular wave sea states are tested in total, each with a corresponding wind condition. The selected cases (in Table 5) are in the normal operational range of the FOWT as representative of a deployment site with a moderate sea state. They are ~~limited to~~ selected to comply with the capability of the setup ~~as the harshest~~ as harsher waves cannot be tested because the

motion response would go beyond what the Hexapod allows in terms of accelerations. Also, the wind speed is capped to the rated value since the wind turbine model cannot operate at above-rated conditions due to the absence of blade-pitch actuation.

Table 5. Load cases for combined wind and wave conditions. The operational irregular waves are from (Krieger et al., 2015) and the corresponding uniform wind speed is capped to rated. All parameters are at full-scale.

Case	Wave sign. height [m]	Wave peak period [s]	Wind speed [m/s]	Rotor speed [rpm]
1	1.38	7	7	6
2	1.67	8	7.1	6.04
3	2.2	8	10.3	8.27
4	3.04	9.5	11.4	9.6
5	4.29	10	11.4	9.6

405 From the motion response PSD in Fig. 10 for an operational wind and wave case with wind speed at the rated value (case 4), it is visible that there are two significant areas of activity. The first is near the natural frequency range of the floating platform, which is towards the lower frequency range; this is also the region where the effects of wind are visible (Larsen and Hanson, 2007). This region is also known to be subjected to effects due to the HIL itself (Fontanella et al., 2023b), which are not investigated in this work. The second is near the wave frequency range, where the activity due to the emulated
410 wave can be observed, the frequency of the highest energy wave is denoted with a dashed line. The responses in the surge, pitch and heave DOFs are more pronounced in this region, this is expected since the wave heading in these test cases is set at 0deg. Finally, the rotor 1P frequency, denoted with the dotted line, shows a significant response in the heave and the roll DOFs compared to other regions of activity and response is present in this frequency in all DOFs. A comparison of the motion response for all the load cases is shown in Fig.11. The motion response increases with rising sea state and wind conditions, and
415 this occurs across the entire frequency range. Case 5 shows outlier behaviour, deviating from the other cases also in DOFs like sway and roll that should be less affected by wind and waves loading. This can be attributed to reaching the limit of the hexapod or the HIL system, or to increased vibrations, and gives an indication of the limit capabilities of the setup. The dynamic response to wind and waves is qualitatively in line with what is found in the literature of HIL studies, such as in Belloli et al. (2020), where similar areas of activity were found, confirming the suitability of the setup for this kind of study.

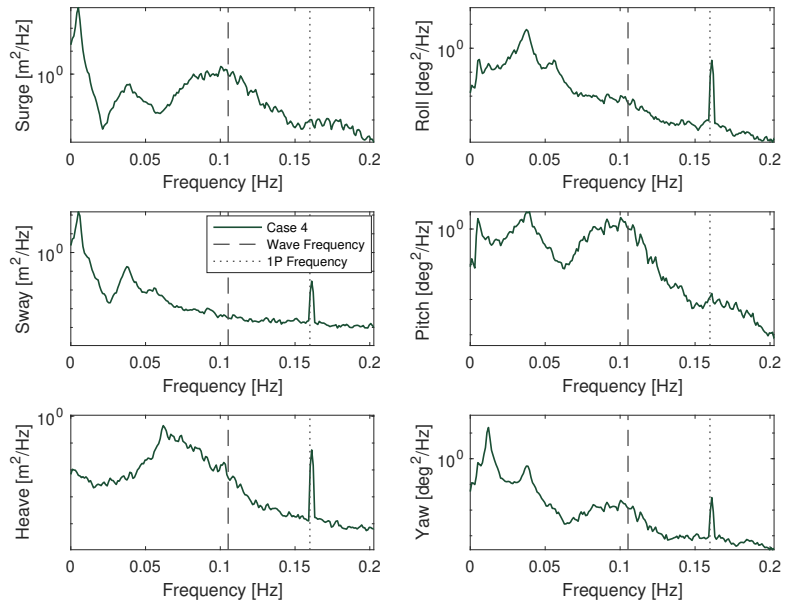


Figure 10. PSD of floater motion response to the combined wind (HIL in *Closed-Loop* configuration) and wave loading for case 4. The results are upscaled.

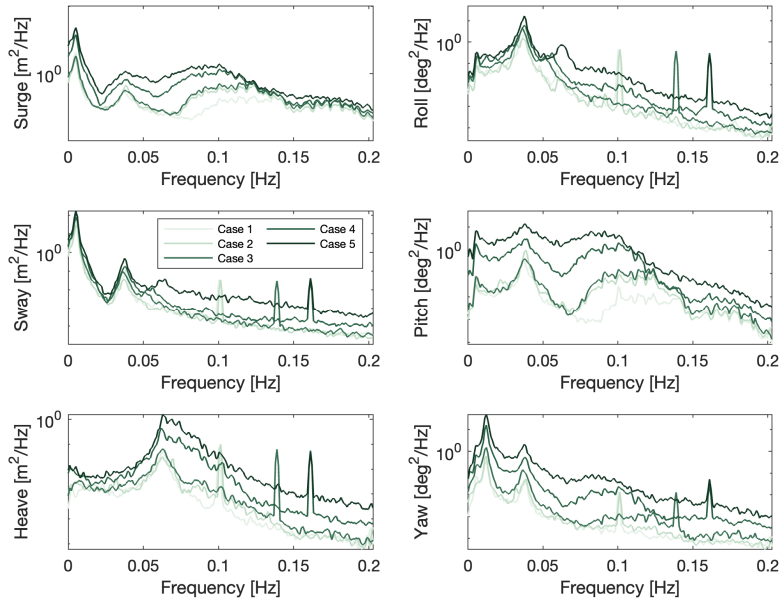


Figure 11. PSD of floater motion response to the combined wind (HIL in *Closed-Loop* configuration) and wave loading for cases 1 to 5. The results are upscaled.

420 5 Conclusions

This work presents a hardware-in-the-loop wind tunnel setup designed to study the coupled aerodynamic and motion response of floating offshore wind turbines. By including the aerodynamic feedback in real-time, the setup enables the study of phenomena such as aerodynamic damping and motion-induced rotor loading that cannot be captured in uncoupled experiments. At the time of writing, only two other wind tunnel HIL setups exist for this purpose, and few experiments have been carried out with
 425 the full dynamic coupling. There is thus a need to develop additional and complementary setups for comparison and advancing experimental investigations on floating turbines.

A key characteristic of the setup presented in this work is its ability to move in six degrees-of-freedom. This allows for the analysis of realistic motions, as encountered offshore, as well as investigating coupling effects between different DOFs. Another important achievement of this work is the development and implementation of a new aerodynamic force correction
 430 methodology, necessary to compensate for scaling inconsistencies in mass and acceleration between the physical and numerical subsystems. The method relies on measured accelerations at the nacelle instead of derived ones from the hexapod position feedback, minimising uncertainty and latency and significantly improving the accuracy of the estimated aerodynamic loads. The assessment of the correction procedure showed that the omission of rotational acceleration terms does not affect roll and pitch responses, and that the induced error in yaw is minimal. The assessment of the HIL architecture confirmed that

435 the correction and actuation chain performs consistently. The open- and closed-loop decay tests matched closely across all degrees-of-freedom, demonstrating that the setup correctly cancels non-aerodynamic loads in real-time.

The setup allowed for a direct experimental estimation of aerodynamic damping. ~~The results quantified~~ An increase in damping of pitch, surge and yaw DOFs is expected, and this setup allows for quantifying it with measured rotor loads. The results shows a 210% increase in pitch damping, a 52% increase in yaw, and a 19% increase in surge under rated operating
 440 conditions, highlighting the role of the rotor aerodynamics in stabilising platform motions. Combined wind and wave tests demonstrated the capability of the setup to reproduce realistic offshore loading conditions. The motion responses in surge, heave, and pitch followed the expected behaviour across the wave frequency range, and the setup remained stable within the operational limits of the hexapod.

In conclusion, this work introduces an assessed experimental HIL framework for FOWT aerodynamic-oriented studies.
 445 It allows for analysing the unsteady aerodynamics of floating wind turbines, as well as comparing with the results of HIL in different facilities (e.g. HIL wind tunnels of different sizes, HIL wave tanks). Future studies will build on these results, extending the methodology to address remaining challenges, such as further improving the accuracy of force estimation and including delay compensation, and exploring the aerodynamic behaviour of new turbine designs under increasingly realistic conditions. The framework also sets the basis for validating high-fidelity numerical models.

450 Appendix A: Analytical formulations

A1 Force correction methodology

As integration to Section 3.1, a more complete analytical formulation of the force correction methodology used in the HIL model is illustrated in this appendix. This is to explain the theory behind the formulation in Eq. 3.

The forces and torques measured by the load cell, under the rigid body assumption, installed under the nacelle can be
 455 analytically expressed as:

$$\begin{aligned}
 F_{meas} = \underbrace{\begin{bmatrix} F_{aero,x} \\ F_{aero,y} \\ F_{aero,z} \end{bmatrix}}_{F_{aero}} + R^{-1} \left(\underbrace{\begin{bmatrix} 0 \\ 0 \\ -M_{rna}g \end{bmatrix}}_{F_{grav}} - \underbrace{\begin{bmatrix} M_{rna}\ddot{x} \\ M_{rna}\ddot{y} \\ M_{rna}\ddot{z} \end{bmatrix}}_{F_{in,trans}} - \underbrace{M_{rna} \left(\begin{bmatrix} \ddot{\phi} \\ \ddot{\theta} \\ \ddot{\psi} \end{bmatrix} \times \left(R \begin{bmatrix} 0 \\ 0 \\ hh \end{bmatrix} \right) \right)}_{F_{in,tang}} - \underbrace{M_{rna} \left(\begin{bmatrix} \dot{\theta}_x \\ \dot{\theta}_y \\ \dot{\theta}_z \end{bmatrix} \times \left(\begin{bmatrix} \dot{\theta}_x \\ \dot{\theta}_y \\ \dot{\theta}_z \end{bmatrix} \times \left(R \begin{bmatrix} 0 \\ 0 \\ h \end{bmatrix} \right) \right) \right)}_{F_{in,centr}} \right)
 \end{aligned}
 \tag{A1}$$

and:

$$T_{meas} = \underbrace{\begin{bmatrix} T_{aero,x} \\ T_{aero,y} \\ T_{aero,z} \end{bmatrix}}_{T_{aero}} - R^{-1} \underbrace{\begin{bmatrix} J_{rna,x} \ddot{\theta}_x \\ J_{rna,y} \ddot{\theta}_y \\ J_{rna,z} \ddot{\theta}_z \end{bmatrix}}_{T_{in,rot}} + \underbrace{\begin{bmatrix} F_{in,x}^* z_{lc} \\ F_{in,y}^* z_{lc} \\ 0 \end{bmatrix}}_{T_{in,trans}}, \quad (A2)$$

where:

- 460 – F_{meas} are the forces measured by the load cell
- T_{meas} are the torques measured by the load cell
- $F_{aero,x}, F_{aero,y}, F_{aero,z}$ are the aerodynamic forces
- $T_{aero,x}, T_{aero,y}, T_{aero,z}$ are the aerodynamic torques
- M_{rna} is the mass of the RNA
- 465 – J_{rna} is the inertia of the RNA
- g is the gravity acceleration
- R is the rotation matrix
- hh is the hub height
- z_{lc} is the distance between the RNA centre of mass and the load cell
- 470 – $\ddot{x}, \ddot{y}, \ddot{z}$ are the acceleration in surge, sway and heave (in the fixed frame, at tower bottom)
- $\ddot{\theta}_x, \ddot{\theta}_y, \ddot{\theta}_z$ are the rotational accelerations in roll, pitch and heave (in the fixed frame)
- * in A2 means already calculated in A1

The accelerations measured by the accelerometer installed at the nacelle can be analytically expressed as:

$$a_{meas} = R^{-1} \cdot \left(\underbrace{\begin{bmatrix} 0 \\ 0 \\ -g \end{bmatrix}}_{a_{grav}} + \underbrace{\begin{bmatrix} \ddot{x} \\ \ddot{y} \\ \ddot{z} \end{bmatrix}}_{a_{trans}} + \underbrace{\left(\begin{bmatrix} \ddot{\theta}_x \\ \ddot{\theta}_y \\ \ddot{\theta}_z \end{bmatrix} \times \left(R \begin{bmatrix} 0 \\ 0 \\ hh \end{bmatrix} \right) \right)}_{a_{tang}} + \underbrace{\left(\begin{bmatrix} \dot{\theta}_x \\ \dot{\theta}_y \\ \dot{\theta}_z \end{bmatrix} \times \left(\begin{bmatrix} \dot{\theta}_x \\ \dot{\theta}_y \\ \dot{\theta}_z \end{bmatrix} \times \left(R \begin{bmatrix} 0 \\ 0 \\ hh \end{bmatrix} \right) \right) \right)}_{a_{centr}} \right), \quad (A3)$$

475 where:

- a_{meas} are the accelerations measured by the accelerometer

– g is the gravity acceleration

– R is the rotation matrix

– hh is the hub height

480 – $\ddot{x}, \ddot{y}, \ddot{z}$ are the acceleration in surge, sway and heave (in the fixed frame, at tower bottom)

– $\ddot{\theta}_x, \ddot{\theta}_y, \ddot{\theta}_z$ are the rotational accelerations in roll, pitch and heave (in the fixed frame)

The formulation of the force correction in Eq. 3 is obtained from here. [It has to be noted that the present formulation neglects gyroscopic effects and does not correct for them.](#)

A2 Rotation matrices

485 Rotation transformation matrices are used in the HIL model. This is necessary because the equation of motion is solved in the fixed frame, while the acceleration and force measurements are taken by sensors attached to the wind turbine, which are in a moving frame. The rotation matrices are first determined to transform from the moving frame to the fixed frame. The rotation matrices are:

490 Yaw rotation:

$$R_z(\psi) = \begin{bmatrix} \cos(\psi) & -\sin(\psi) & 0 \\ 3\sin(\psi) & \cos(\psi) & 0 \\ 0 & 0 & 1 \end{bmatrix}$$

Pitch rotation:

$$R_y(\theta) = \begin{bmatrix} \cos(\theta) & 0 & \sin(\theta) \\ 0 & 1 & 0 \\ -\sin(\theta) & 0 & \cos(\theta) \end{bmatrix}$$

Roll rotation:

495 $R_x(\phi) = \begin{bmatrix} 1 & 0 & 0 \\ 0 & \cos(\phi) & -\sin(\phi) \\ 0 & \sin(\phi) & \cos(\phi) \end{bmatrix}$

The order of rotations, or the Euler sequence, plays a crucial role in the transformation matrix, as different sequences can yield different results. For a 6-DOF system, the transformation matrices are multiplied threefold, so the rotation order must be set correctly to avoid amplifying errors. The generally accepted order of rotation is the Yaw-Pitch-Roll transformation. When applying this transformation, the matrices are multiplied in the Roll-Pitch-Yaw order. The final rotation matrix is:

500 $R = R_z(\psi)R_y(\theta)R_x(\phi)$ (A4)

This order of rotation is used to transform from a rotated reference frame to a fixed reference frame. The inverse of the transformation is used to convert from a fixed frame to a moving frame.

A3 Force rotation and transport

The forces have to be transformed from the rotating frame they are measured into a fixed frame. The equation of motion is solved at the MSL (mean sea level), i.e. at the tower base. Hence, the transportation of the forces to the tower base is also necessary. The aerodynamic force and torque used in the equation of motion ($F_{aero,tb}, T_{aero,tb}$, where tb stands for tower-bottom) are:

$$F_{aero,tb} = R \cdot F_{aero} \quad (A5)$$

$$T_{aero,tb} = \begin{bmatrix} F_{aero,f}(x) \\ -F_{aero,f}(y) \\ F_{aero,f}(z) \end{bmatrix} \times \begin{bmatrix} pos_{tt}(x) \\ -pos_{tt}(y) \\ pos_{tt}(z) \end{bmatrix} + T_{aero} \quad (A6)$$

A4 Equation of motion

A complete formulation of the equation of motion of the rigid body dynamics of FOWTs is shown here to complement Eq. 4:

$$(M_s + A)\ddot{x} + R_{visc}\dot{x} + K_{grav} + K_{hst} + K_{moor}x = F_{rad} + F_{diff,1} + F_{aero, est.}, \quad (A7)$$

where:

- 515 – M_s is the structural mass and inertia matrix of the whole FOWT (rotor included)
- A is the infinite-frequency hydrodynamic added mass
- R_{visc} is the linear viscous hydrodynamic damping matrix
- K_{grav} is the gravitational restoring stiffness matrix of the entire FOWT (rotor included)
- K_{hst} is the hydrostatic restoring stiffness matrix
- 520 – K_{moor} is the linearized mooring stiffness matrix
- F_{rad} is the calculated radiation force (with state-space approximation)
- $F_{diff,1}$ is the generated first order diffraction force
- $F_{aero, est.}$ is the aerodynamic force estimated from the measures

A5 Hexapod motion tracking

525 The hexapod robot is a commercial component. It is however important to verify its motion tracking performance and this is done by observing the time history and computing the transfer function of the position setpoint sent to the hexapod and the actual position received as feedback from the hexapod. A wave case (case 4) is considered and surge motion are used to evaluate the translation tracking and pitch motion to evaluate the rotation tracking.

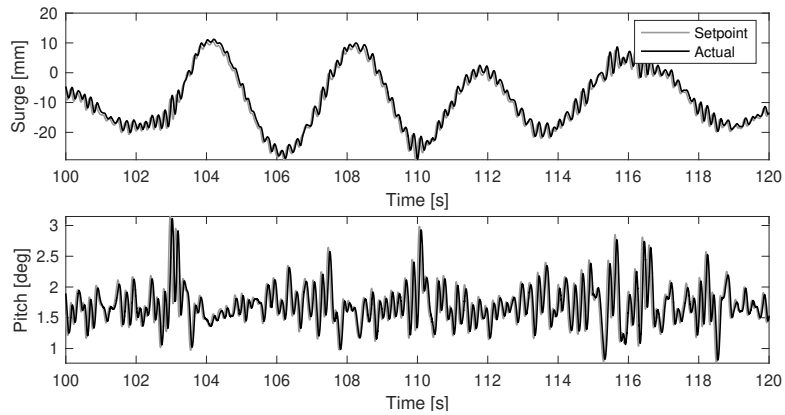


Figure A1. Time history of surge and pitch setpoint and actual hexapod position for a wave case.

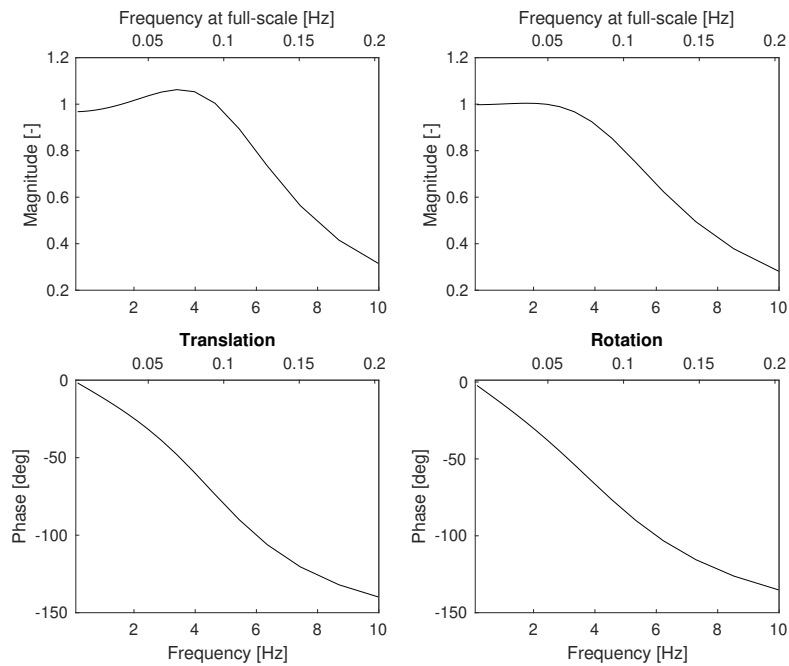


Figure A2. Bode diagram of ~~translational~~ motion tracking.

~~Bode diagram of rotational motion tracking.~~

530 A6 Force correction analysis

The analysis of the force correction procedure is expanded here, showing it for all the directions and for some illustrative cases with wind. In all the following plots, light blue lines indicate measured force signals, red lines visualise the correction action, the green lines indicate the estimated aerodynamic force signals, and the black lines show the main DOF(s) motion. The yaw case in Fig. A5 has no correction action. In the cases with wind in Fig. A6 and Fig. A7, the estimated aerodynamic force is not
 535 null.

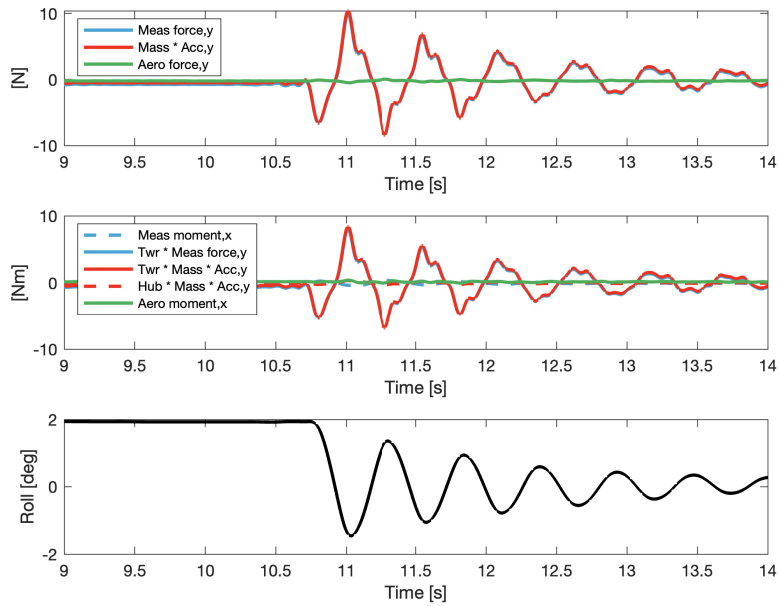


Figure A3. Force correction in the lateral direction for a roll decay without wind.

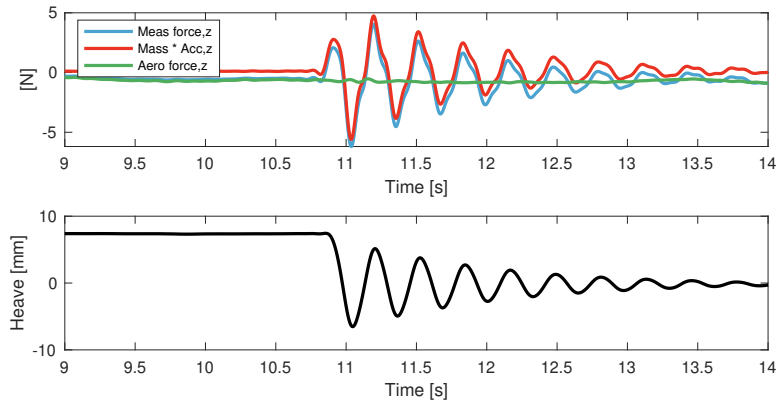


Figure A4. Force correction in the vertical direction for a heave decay without wind.

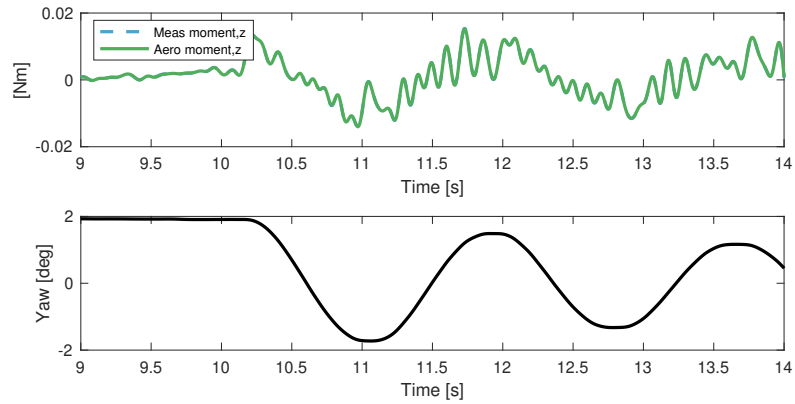


Figure A5. Moment in the yaw direction for a yaw decay without wind.

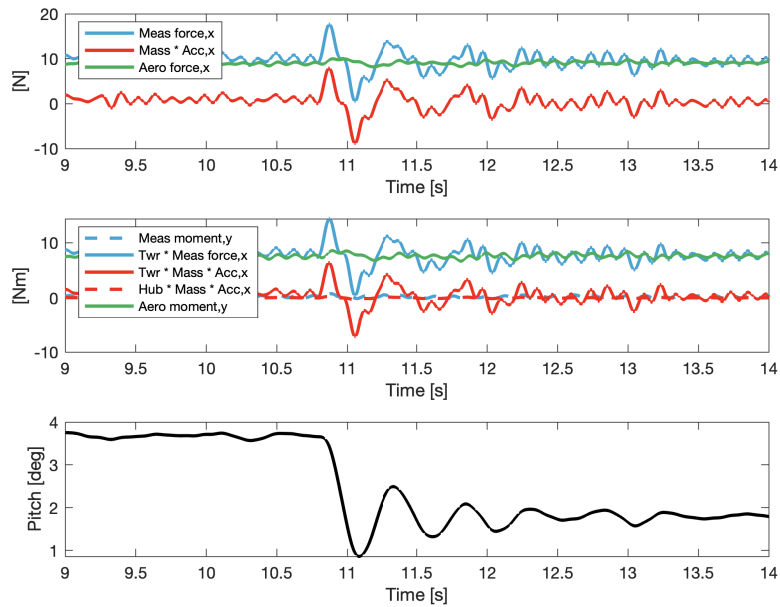


Figure A6. Force correction in the along-wind direction for a pitch decay with rated wind and spinning rotor.

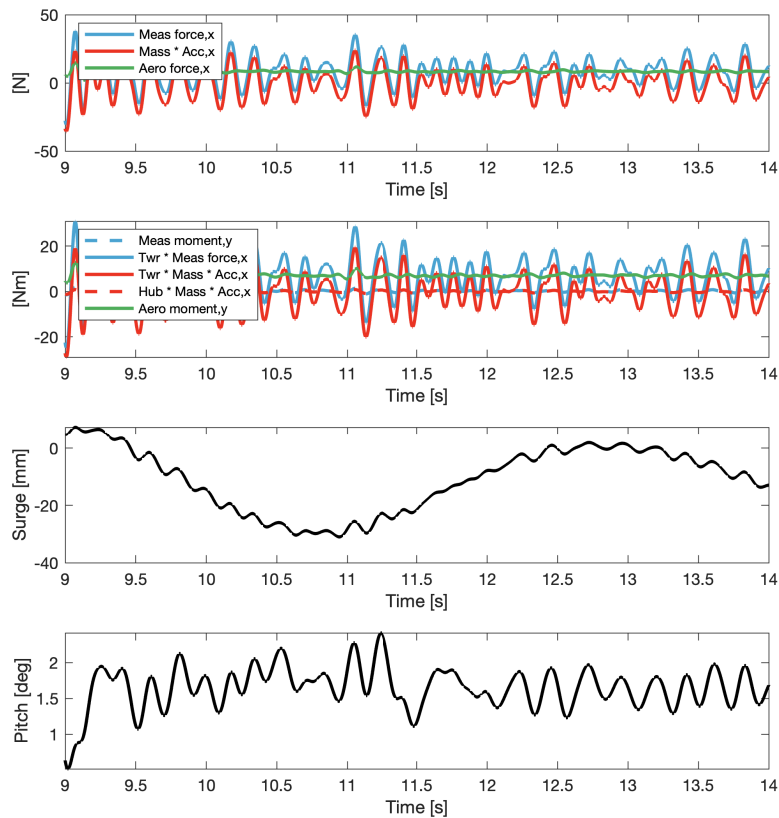


Figure A7. Force correction in the along-wind direction for wind and wave case 4.

Data availability. The dataset is accessible upon request to the authors.

Author contributions. FT and AV imagined the scope of the work and designed the experimental campaign. FT developed the experimental setup. FT developed the numerical models and carried out the tests. FT performed the analyses of the results. FT and AV performed the literature review. FT prepared the manuscript, including contributions from the co-author, and interpreted the results. AV reviewed the manuscript.

540

Competing interests. The authors declare that they have no conflict of interest.

Acknowledgements. The research is partially funded by the Dutch National Research Council (NWO) within the project HybridLabs (NWA.1518.22.066) of the research programme Dutch Research Agenda – research along NWA routes by consortia and through the Talent Programme Vidi scheme (project number 19675). The authors would also like to acknowledge Shakthi Thinakaran for her contribution to this work with her master’s thesis and her participation in the experimental tests.

References

- Armesto, J. A., Jurado, A., Guanche, R., Couñago, B., Urbano, J., and Serna, J.: TELWIND: Numerical Analysis of a Floating Wind Turbine Supported by a Two Bodies Platform, in: Volume 10: Ocean Renewable Energy, American Society of Mechanical Engineers, ISBN 978-0-7918-5131-9, <https://doi.org/10.1115/OMAE2018-77587>, 2018.
- 550 Azcona, J., Bouchotrouch, F., González, M., Garcíandía, J., Munduate, X., Kelberlau, F., and Nygaard, T. A.: Aerodynamic Thrust Modelling in Wave Tank Tests of Offshore Floating Wind Turbines Using a Ducted Fan, *Journal of Physics: Conference Series*, 524, 012089, <https://doi.org/10.1088/1742-6596/524/1/012089>, 2014.
- Azcona, J., Bouchotrouch, F., and Vittori, F.: Low-frequency dynamics of a floating wind turbine in wave tank-scaled experiments with SiL hybrid method, *Wind Energy*, 22, 1402–1413, <https://doi.org/10.1002/we.2377>, 2019.
- 555 Bachynski, E. E., Thys, M., Sauder, T., Chabaud, V., and Sæther, L. O.: Real-Time Hybrid Model Testing of a Braceless Semi-Submersible Wind Turbine: Part II — Experimental Results, in: Volume 6: Ocean Space Utilization; Ocean Renewable Energy, American Society of Mechanical Engineers, ISBN 978-0-7918-4997-2, <https://doi.org/10.1115/OMAE2016-54437>, 2016.
- Bak, C., Zahle, F., Bitsche, R., Kim, T., Yde, A., Henriksen, L. C., Nata-rajana, A., and Hansen, M. H.: Department of Wind Energy I-Report Description of the DTU 10 MW Reference Wind Turbine, 2013.
- 560 Bayati, I., Belloli, M., Bernini, L., and Zasso, A.: Wind Tunnel Wake Measurements of Floating Offshore Wind Turbines, *Energy Procedia*, 137, 214–222, <https://doi.org/10.1016/j.egypro.2017.10.375>, 2017.
- Bayati, I., Facchinetti, A., Fontanella, A., and Belloli, M.: 6-DoF hydrodynamic modelling for wind tunnel hybrid/HIL tests of FOWT: the real-time challenge, in: International Conference on Offshore Mechanics and Arctic Engineering, vol. 51319, p. V010T09A078, American Society of Mechanical Engineers, <https://doi.org/10.1115/OMAE2018-77804>, 2018a.
- 565 Bayati, I., Facchinetti, A., Fontanella, A., Giberti, H., and Belloli, M.: A wind tunnel/HIL setup for integrated tests of Floating Offshore Wind Turbines, *Journal of Physics: Conference Series*, 1037, 052025, <https://doi.org/10.1088/1742-6596/1037/5/052025>, 2018b.
- Belloli, M., Bayati, I., Facchinetti, A., Fontanella, A., Giberti, H., Mura, F. L., Taruffi, F., and Zasso, A.: A hybrid methodology for wind tunnel testing of floating offshore wind turbines, *Ocean Engineering*, 210, <https://doi.org/10.1016/j.oceaneng.2020.107592>, 2020.
- Bredmose, H., Lemmer, F., Borg, M., Pegalajar-Jurado, A., Mikkelsen, R. F., Larsen, T. S., Fjelstrup, T., Yu, W., Lomholt, A. K., Boehm, L., and Armendariz, J. A.: The Triple Spar campaign: Model tests of a 10MW floating wind turbine with waves, wind and pitch control, in: *Energy Procedia*, vol. 137, pp. 58–76, Elsevier Ltd, ISSN 18766102, <https://doi.org/10.1016/j.egypro.2017.10.334>, 2017.
- 570 Brodtkorb, P. A., Johannesson, P., Lindgren, G., Rychlik, I., Rydén, J., and Sjö, E.: WAFO-a Matlab toolbox for analysis of random waves and loads, in: ISOPE International Ocean and Polar Engineering Conference, pp. ISOPE-I, isope, 2000.
- Cermelli, C. and Aubault, A.: OTC 20674 Qualification of a Semi-Submersible Floating Foundation for Multi-Megawatt Wind Turbines, Tech. rep., <http://onepetro.org/OTCONF/proceedings-pdf/10OTC/All-10OTC/OTC-20674-MS/1719099/otc-20674-ms.pdf/1>, 2010.
- 575 Cummins, W. et al.: The impulse response function and ship motions, 1962.
- Doisenbant, G., Boulluec, M. L., Scolan, Y.-M., and Guyot, M.: Application to reduced scale model testing, *Wind Engineering*, 42, 108–114, <https://www.jstor.org/stable/90019972>, 2018.
- Dong, J. and Viré, A.: The aerodynamics of floating offshore wind turbines in different working states during surge motion, *Renewable*
- 580 *Energy*, 195, 1125–1136, <https://doi.org/10.1016/j.renene.2022.06.016>, 2022.

- Duarte, T., Alves, M., Jonkman, J., and Sarmiento, A.: State-Space Realization of the Wave-Radiation Force Within FAST, vol. Volume 8: Ocean Renewable Energy of *International Conference on Offshore Mechanics and Arctic Engineering*, p. V008T09A021, <https://doi.org/10.1115/OMAE2013-10375>, 2013.
- Fontanella, A., Da Pra, G., and Belloli, M.: Integrated Design and Experimental Validation of a Fixed-Pitch Rotor for Wind Tunnel Testing, *Energies*, 16, <https://doi.org/10.3390/en16052205>, 2023a.
- Fontanella, A., Facchinetti, A., Daka, E., and Belloli, M.: Modeling the coupled aero-hydro-servo-dynamic response of 15 MW floating wind turbines with wind tunnel hardware in the loop, *Renewable Energy*, 219, 119–442, <https://doi.org/10.1016/j.renene.2023.119442>, 2023b.
- Goupee, A. J., Fowler, M. J., Kimball, R. W., Helder, J., and de Ridder, E.-J.: Additional Wind/Wave Basin Testing of the DeepCwind Semi-Submersible With a Performance-Matched Wind Turbine, in: Volume 9B: Ocean Renewable Energy, American Society of Mechanical Engineers, ISBN 978-0-7918-4554-7, <https://doi.org/10.1115/OMAE2014-24172>, 2014a.
- Goupee, A. J., Koo, B. J., Kimball, R. W., Lambrakos, K. F., and Dagher, H. J.: Experimental comparison of three floating wind turbine concepts, *Journal of Offshore Mechanics and Arctic Engineering*, 136, <https://doi.org/10.1115/1.4025804>, 2014b.
- Jiang, Z., Wen, B., Chen, G., Tian, X., Li, J., Ouyang, D., Peng, Z., Dong, Y., and Zhou, G.: Real-time hybrid test method for floating wind turbines: Focusing on the aerodynamic load identification, *Journal of Ocean Engineering and Science*, 10, 449–461, <https://doi.org/10.1016/j.joes.2024.06.002>, 2025.
- Jonkman, J. M. and Buhl, M. L.: FAST User's Guide: Technical Report, 2005.
- Krieger, A., Ramachandran, G. K. V., L., V., Gómez Alonso, P., González Almería, G., Berque, J., and Aguirre, G.: LIFES50+ D7.2: Design basis, 2015.
- Larsen, T. J. and Hanson, T. D.: A method to avoid negative damped low frequent tower vibrations for a floating, pitch controlled wind turbine, in: *Journal of Physics: Conference Series*, vol. 75, ISSN 17426596, <https://doi.org/10.1088/1742-6596/75/1/012073>, 2007.
- Lemmer, F., Amann, F., Raach, S., and Schlipf Swe, D.: Definition of the SWE-TripleSpar Floating Platform for the DTU 10MW Reference Wind Turbine, Tech. rep., 2016.
- Lemmer, F., Raach, S., Schlipf, D., Faerron-Guzmán, R., and Cheng, P. W.: FAST model of the SWE-TripleSpar floating wind turbine platform for the DTU 10MW reference wind turbine, <https://doi.org/10.18419/DARUS-514>, 2020.
- Lignarolo, L.: On the turbulent mixing in horizontal axis wind turbine wakes, Ph.D. thesis, Delft University of Technology, 2016.
- Oguz, E., Clelland, D., Day, A. H., Incecik, A., López, J. A., Sánchez, G., and Almeria, G. G.: Experimental and numerical analysis of a TLP floating offshore wind turbine, *Ocean Engineering*, 147, 591–605, <https://doi.org/10.1016/j.oceaneng.2017.10.052>, 2018.
- Papi, F., Jonkman, J., Robertson, A., and Bianchini, A.: Going beyond BEM with BEM: an insight into dynamic inflow effects on floating wind turbines, *Wind Energy Science*, 9, 1069–1088, <https://doi.org/10.5194/wes-9-1069-2024>, 2024.
- Ramachandran, G., Vita, L., Krieger, A., and Mueller, K.: Design basis for the feasibility evaluation of four different floater designs, *Energy Procedia*, 137, 186–195, 2017.
- Robertson, A. N., Jonkman, J. M., Goupee, A. J., Coulling, A. J., Prowell, I., Browning, J., Masciola, M. D., and Molta, P.: Summary of Conclusions and Recommendations Drawn From the DeepCwind Scaled Floating Offshore Wind System Test Campaign, vol. Volume 8: Ocean Renewable Energy of *International Conference on Offshore Mechanics and Arctic Engineering*, p. V008T09A053, <https://doi.org/10.1115/OMAE2013-10817>, 2013.
- Ruzzo, C., Muggiasca, S., Malara, G., Taruffi, F., Belloli, M., Collu, M., Li, L., Brizzi, G., and Arena, F.: Scaling strategies for multi-purpose floating structures physical modeling: state of art and new perspectives, *Applied Ocean Research*, 108, <https://doi.org/10.1016/j.apor.2020.102487>, 2021.

- Schulz, C. W., Netzband, S., Özinan, U., Cheng, P. W., and Abdel-Maksoud, M.: Wind turbine rotors in surge motion: new insights into unsteady aerodynamics of floating offshore wind turbines (FOWTs) from experiments and simulations, *Wind Energy Science*, 9, 665–695, <https://doi.org/10.5194/wes-9-665-2024>, 2024.
- Shi, W., Fu, J., Ren, Z., Jiang, Z., Wang, T., Cui, L., and Li, X.: Real-time hybrid model tests of floating offshore wind turbines: Status, challenges, and future trends, *Applied Ocean Research*, 141, <https://doi.org/10.1016/j.apor.2023.103796>, 2023.
- Taruffi, F., Combette, R., and Viré, A.: Experimental and CFD analysis of a floating offshore wind turbine under imposed motions, in: *Journal of Physics: Conference Series*, vol. 2767, p. 062010, IOP Publishing, 2024a.
- Taruffi, F., Novais, F., and Viré, A.: An experimental study on the aerodynamic loads of a floating offshore wind turbine under imposed motions, *Wind Energy Science*, 9, 343–358, <https://doi.org/10.5194/wes-9-343-2024>, 2024b.
- Thys, M., Chabaud, V., Sauder, T., Eliassen, L., Sæther, L. O., and Magnussen, B.: Real-Time Hybrid Model Testing of a Semi-Submersible 10MW Floating Wind Turbine and Advances in the Test Method, in: *ASME 2018 1st International Offshore Wind Technical Conference*, American Society of Mechanical Engineers, ISBN 978-0-7918-5197-5, <https://doi.org/10.1115/IOWTC2018-1081>, 2018.
- van Kuik, G. A. M., Peinke, J., Nijssen, R., Lekou, D., Mann, J., Sørensen, J. N., Ferreira, C., van Wingerden, J. W., Schlipf, D., Gebraad, P., Polinder, H., Abrahamsen, A., van Bussel, G. J. W., Sørensen, J. D., Tavner, P., Bottasso, C. L., Muskulus, M., Matha, D., Lindeboom, H. J., Degraer, S., Kramer, O., Lehnhoff, S., Sonnenschein, M., Sørensen, P. E., Küenneke, R. W., Morthorst, P. E., and Skytte, K.: Long-term research challenges in wind energy – a research agenda by the European Academy of Wind Energy, *Wind Energy Science*, 1, 1–39, <https://doi.org/10.5194/wes-1-1-2016>, 2016.
- Viselli, A. M., Goupee, A. J., and Dagher, H. J.: Model Test of a 1:8-Scale Floating Wind Turbine Offshore in the Gulf of Maine¹, *Journal of Offshore Mechanics and Arctic Engineering*, 137, <https://doi.org/10.1115/1.4030381>, 2015.
- Vittori, F., Azcona, J., Eguinoa, I., Pires, O., Rodríguez, A., Morató, A., Garrido, C., and Desmond, C.: Model tests of a 10 MW semi-submersible floating wind turbine under waves and wind using hybrid method to integrate the rotor thrust and moments, *Wind Energy Science*, 7, 2149–2161, <https://doi.org/10.5194/wes-7-2149-2022>, 2022.
- Zhao, Y. s., She, X. h., He, Y. p., Yang, J. m., Peng, T., and Kou, Y. f.: Experimental Study on New Multi-Column Tension-Leg-Type Floating Wind Turbine, *China Ocean Engineering*, 32, 123–131, <https://doi.org/10.1007/s13344-018-0014-0>, 2018.